TABLE 1. Characteristics of Patients with Bronchial R1 Disease

Characteristics	No. (%)
Sex	
Male	58 (78)
Female	16 (22)
Age	
Range (yr)	39–83
Median (yr)	66
Pathological stage	
0	1 (1)
I	6 (8)
II	10 (14)
III	52 (70)
IV	5 (7)
Histology	
Adenocarcinoma	35 (47)
Squamous cell carcinoma	34 (46)
Large cell carcinoma	3 (5)
Adenosquamous cell carcinoma	1 (1)
Giant cell carcinoma	1 (1)
Pulmonary resection	
Pneumonectomy	17 (23)
With carinal resection	1
Bilobectomy	16 (22)
With bronchial resection	3
Lobectomy	41 (55)
With bronchial resection	15
Type of bronchial R1	
Direct extension	11 (15)
Peribronchial extension	54 (73)
Carcinoma in situ	9 (12)
Postoperative RT	
Yes	21 (28)
No	53 (72)

Morphology of R1 Disease

Patients with bronchial R1 were classified into the following three categories according to the residual tumor pattern: (1) Direct extension (DIR, $n = 11$, Figure 1*A*), characterized by direct invasive extension of the main tumor proximally in the bronchial wall; (2) Peribronchial extension (PER, $n = 54$, Figure 1*B*), which included tumor infiltration into the peribronchial connective tissues, lymphatic permeation by peribronchial lymphatic vessels, or extracapsular infiltration of the metastatic lymph nodes; (3) Carcinoma in situ (CIS, $n = 9$, Figure 1*C*), characterized by in situ extension of the main tumor, which continued up to the bronchial resection margin. All patients with CIS lesion had squamous cell carcinoma.

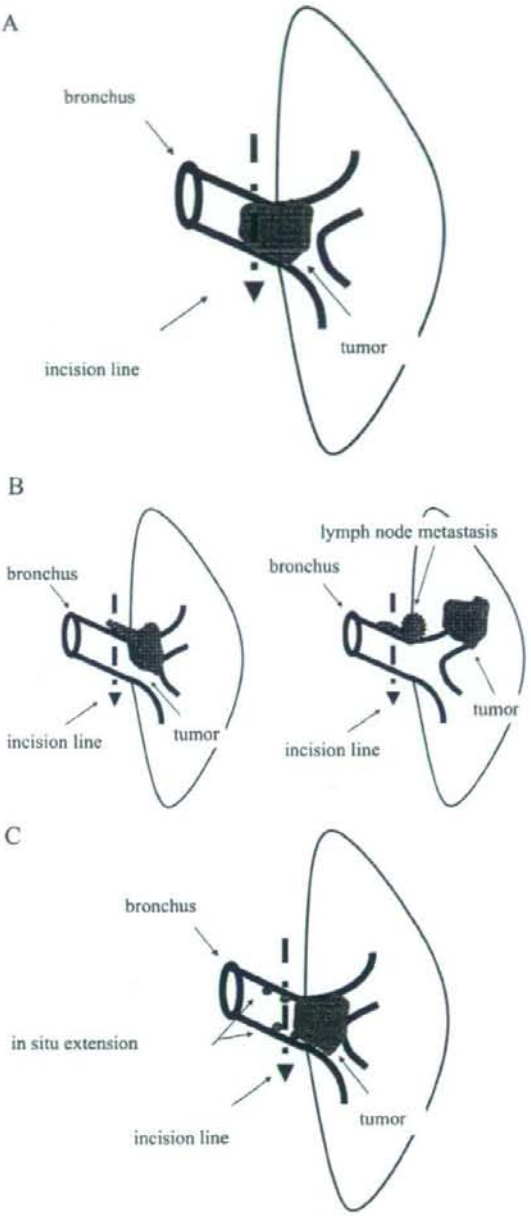

FIGURE 1. Schemas of bronchial R1 (*A*) direct extension, (*B*) peribronchial extension, and (*C*) carcinoma in situ.

Postoperative Therapy

Postoperative radiotherapy was administered for 21 patients (5 with DIR, 11 with PER, and 5 with CIS). Patients in poor physical condition or with advanced disease did not receive radiotherapy. The total radiation dose ranged from 29 to 60 Gy (median, 50 Gy). None of the patients in this study received postoperative chemotherapy.

Prognosis

Tumor recurrence was described as local or distant. Local recurrence was defined as any recurrent disease within the ipsilateral hemithorax or mediastinum. Recurrence was diagnosed by bronchoscopic biopsy or noninvasive diagnostic procedures such as radiography, computerized tomography, magnetic resonance imaging, or bone scan.

Statistical Analysis

Survival curves were estimated by the product limit method of Kaplan and Meier, and the differences in survival were tested with log-rank analysis. The length of survival was defined as the interval between the day of initial operation and the day of death or last follow-up. Observation was censored at the last follow-up when patients were alive, and all deaths, including operative deaths, were considered events. The median follow-up period for the 12 surviving patients was 51 months. The χ^2 test was performed to evaluate the correlation between bronchial R1 morphology and recurrence. Statistical significance was set at $p < 0.05$.

RESULTS

The median survival time for all patients with bronchial R1 was 14 months, with actual survival rates of 57, 26, and 14% at 1, 3, and 5 years, respectively (Figure 2). According to the bronchial R1 morphology, the 5-year survival rates of patients with DIR, PER, and CIS were 0, 10, and 63%, respectively (Figure 3). Patients with CIS fared significantly better than did patients with the other types of bronchial R1 (DIR versus CIS, $p = 0.0006$; PER versus CIS, $p = 0.0009$). On the other hand, we detected no difference in the prognoses of patients with DIR and PER ($p = 0.1753$). Among patients with DIR and PER, histologic classification or pathologic nodal status did not affect the probability of survival (squamous cell carcinoma versus nonsquamous cell carcinoma, $p = 0.4227$; pN0–1 versus pN2, $p = 0.1768$).

During follow-up, progressive disease developed in 43 (58%), 20 patients were free of disease, and details of predeath status were not known for 11 patients. Correlations between the first site of relapse and bronchial R1 morphology are shown in Table 2. In patients with CIS, local recurrence developed in only one patient (11%) and no distant metastasis was observed. On the other hand, recurrence rates of patients with DIR (54%) and PER (66%) were significantly higher than that of patients with CIS ($p = 0.036$, $p = 0.006$, respectively), and 34 of the 42 recurrences (81%) included distant metastases. Among 21 patients treated with postoperative radiotherapy, 12 patients relapsed (Table 3). Despite the radiotherapy, local recurrence developed in 4 patients (19%). Furthermore, in DIR and PER group, half of the patients that received radiotherapy (8 of 16) had recurrences at the distant sites. Prognosis was not affected by postoperative radiotherapy ($p = 0.667$, Figure 4).

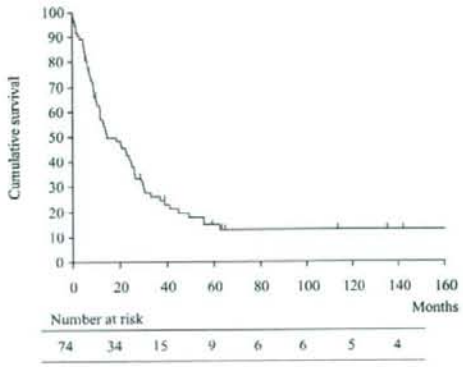

FIGURE 2. Cumulative survival for the entire group.

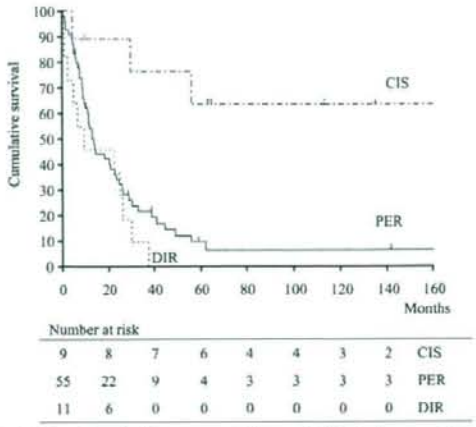

FIGURE 3. Survival by type of bronchial R1 disease. Carcinoma in situ (CIS) versus direct extension (DIR), $p = 0.0006$; CIS versus peribronchial extension (PER), $p = 0.0009$, DIR versus PER, $p = 0.18$.

TABLE 2. First Site of Relapse in Patients with Bronchial R1

	DIR ($n = 11$) (%)	PER ($n = 54$) (%)	CIS ($n = 9$) (%)
Local	2 (18)	6 (11)	1 (11)
Distant	4 (36)	26 (48)	0 (0)
Local + distant	0 (0)	4 (7)	0 (0)
Total	6 (54)	36 (66)	1 (11)

DIR, direct extension; PER, peribronchial extension; CIS, carcinoma in situ.

TABLE 3. First Site of Relapse in 21 Patients Undergoing Postoperative Radiotherapy

	DIR ($n = 5$) (%)	PER ($n = 11$) (%)	CIS ($n = 5$) (%)
Local	1 (20)	2 (18)	1 (20)
Distant	2 (40)	5 (45)	0 (0)
Local + distant	0 (0)	1 (9)	0 (0)
Total	3 (60)	8 (72)	1 (20)

DIR, direct extension; PER, peribronchial extension; CIS, carcinoma in situ.

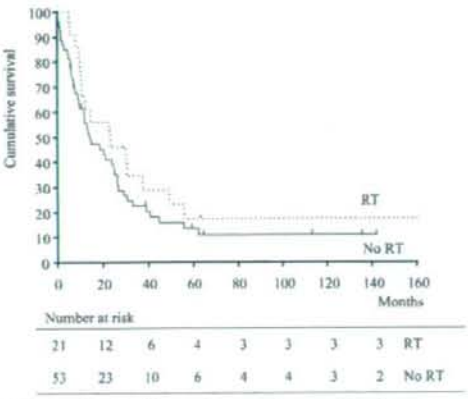

FIGURE 4. Survival in patients with or without postoperative radiotherapy (RT). RT versus non-RT, $p = 0.667$.

BPF developed in six patients (8.1%), 3 of the 11 patients with DIR (27%) and 3 of the 54 patients with PER (5.6%). BPF formation was not detected in patients with CIS. One of the six patients with BPF was treated with postoperative radiotherapy. The mortality rate of patients with BPF was 50% (3 of 6).

DISCUSSION

Gross residual tumors at the resection margin adversely affect the outcome of patients with non-small cell lung cancer; patients with microscopic residual disease at a bronchial resection margin tend to survive longer than do patients with residual gross disease.[3] The incidence of bronchial R1 resection in this study (1.6%) was slightly lower than that reported in the literature (2.6–5.4%).[5,7–11] In our clinical practice, we find that the incidence of cancer arising in the periphery of lung is increasing, therefore the incidence of bronchial R1 disease is less than that reported for this study.

The reported three-year survival rate of patients with bronchial R1 varies from 24 to 40%,[7,10] and the 3-year survival rate detected in this series fell within this range (26%). Because of the heterogeneity of bronchial R1 disease, many authors classify the pattern of bronchial R1 and evaluate prognoses according to these patterns.[5–8,10–12] Soorae and Stevenson[12] analyzed the morphology of microscopic residual tumor at the resected end of bronchus, and classified bronchial R1 disease into four patterns: direct extension of the main tumor mass proximally in the bronchial wall; lymphatic permeation through peribronchial and submucosal lymphatic vessels; extension through parabronchial tissue; and in situ extension. In their study, 15 of 64 patients with bronchial R1 disease survived for more than 5 years. The long-term survivors consisted of seven patients with in situ extension, 7 with DIR, and one with in parabronchial extension. There were no long-term survivors among patients with lymphatic permeation. Therefore, they concluded that bronchial R1 morphology was associated with outcome. Several other studies, including ours, have used the same classification scheme when analyzing patients with bronchial R1.[5–8,10,11]

Among the different morphologies of R1 disease, CIS has been reported to be a favorable indicator of prognosis.[6,8] Snijder et al.[8] analyzed the outcomes of patients with resected stage I disease with bronchial R1 and found no difference in survival between patients with residual CIS and the same-stage R0 patients. Massard et al.[6] reported that cancer-related death was observed in only 5 of 20 patients with CIS (distant metastases in three, combined local recurrence and distant metastases in one, and second primary lung cancer in one). In previous studies, the cause of good prognosis of patients with residual CIS disease was speculated to be: (1) spontaneous regression of residual neoplastic cells caused by smoking cessation; (2) interference with nutrition; (3) local scarring phenomena; or (4) unknown immunologic pathways.[8,12] In our study, the 5-year survival rate of patients with CIS was significantly higher than that of patients with the other two morphologic subtypes (DIR and PER). Cancer-related death occurred in only one of nine patients with CIS. In addition, four of eight patients without recurrence had no postoperative radiotherapy. According to these observations, the prognostic impact of residual CIS disease was different from that of the other types of R1 disease. The role of postoperative radiotherapy for residual CIS disease needs to be further refined. Some patients with CIS disease might be followed up with observation only. Otherwise, the indication for radiotherapy should be determined according to the amount of residual tumor.

We found no difference in the prognoses of patients with either DIR or PER. Among patients with such morphologic subtypes, neither tumor histology nor stage was associated with prognosis. Previous studies have reported prognostic differences related to the pattern of bronchial R1, disease stage, or histology.[5,7,9,10] Liewald et al.[10] reported that the prognosis for patients with extramucosal microscopic residual disease (infiltrating by peribronchial lymphatics or connective tissue) was worse than that for patients with mucosal microscopic residual disease (spreading directly along endobronchial pathway). Others have found prognostic differences associated with disease stage, histology, or presence of lymphangiosis carcinomatosa at the bronchial resection margin.[5,7,9] Nevertheless, according to our analysis, the presence of bronchial R1 disease, except for CIS, was latently associated with disease advancement regardless of tumor histology and stage.

There is no established standard of care for bronchial R1 disease. Several authors have noted that local recurrence develops more often in patients with bronchial R1 than in patients without residual tumor.[6–11] Some of these studies recommended repeated resection for selected cases to prevent local recurrence.[7,8,10,11] Nevertheless, 34 of 42 relapsed patients in our study (81%) with DIR or PER disease had distant metastases, and local therapy such as postoperative radiation did not affect the survival. Therefore, postoperative local therapy might not improve overall survival, since the local therapy does not control distant metastases. The benefit of postoperative local therapy for patients with DIR or PER disease should be considered limited.

In this series, the 8.1% incidence of BPF in patients with R1 disease exceeded that of patients without residual tumor at our hospital (1.5%).[14] Previous studies have reported that the high incidence of BPF was the cause of high mortality rate of patients with bronchial R1 disease.[7,12] Some have speculated that the occurrence of BPF might be related to the presence of residual tumor in the bronchial mucosa.[7,11,12] Based on this study, in which there was no BPF in patients with CIS, in situ extension of tumor cells at the bronchial stump might not be responsible for fistula formation. On the other hand, full thickness invasion to the bronchial partition, which is seen in DIR or PER pattern disease, might promote BPF formation.

We conclude that residual tumor morphology influences the prognosis of patients with bronchial R1 disease after lung cancer resection. The outcomes of patients with CIS are different from those of patients with DIR and PER. The morphology of the residual disease at the resected margin should play an important role in planning postoperative management for patients with bronchial R1.

REFERENCES

1. Pitz CCM, Brutel de la Rivière A, Elbers HRJ, et al. Result of resection of T3 non-small cell lung cancer invading the mediastinum or main bronchus. *Ann Thorac Surg* 1996;62:1016–1020.
2. Ginsberg RJ, Martini N, Zaman M, et al. Influence of surgical resection and brachytherapy in the management of superior sulcus tumor. *Ann Thorac Surg* 1994;57:1440–1445.
3. Shields TM. The fate of patients after incomplete resection of bronchial carcinoma. *Surg Gynecol Obstet* 1974;139:569–572.
4. Sobin LH, Wittekind C. International union against cancer. TNM Classification of Malignant Tumours, 6th Ed. New York: Wiley-Liss, 2002.
5. Passlick B, Sitar I, Sienel W, et al. Significance of lymphangiosis carcinomatosa at the bronchial resection margin in patients with non-small cell lung cancer. *Ann Thorac Surg* 2001;72:1160–1164.
6. Massard G, Doddoli C, Gasser B, et al. Prognostic implications of a positive bronchial resection margin. *Eur J Cardiothorac Surg* 2000;17: 557–565.
7. Ghiribell C, Voltolini L, Paladini P, et al. Treatment and survival after lung resection for non-small cell lung cancer in patients with microscopic residual disease at the bronchial stump. *Eur J Cardiothorac Surg* 1999;17:555–559.
8. Snijder R, Brutel de la Rivière A, Elbers HJJ, et al. Survival in resected stage I lung cancer with residual tumor at the bronchial resection margin. *Ann Thorac Surg* 1998;65:212–216.
9. Gebitekin C, Gupta NK, Satur MR, et al. Fate of patients with residual tumour at the bronchial resection margin. *Eur J Cardiothorac Surg* 1994;8:339–344.
10. Liewald F, Hatz RA, Dieneman H, et al. Importance of microscopic residual disease at the bronchial margin after resection for non-small-cell carcinoma of the lung. *J Thorac Cardiovasc Surg* 1992;104:408–412.
11. Kaiser LR, Fleshner P, Keller S, et al. Significance of extramucosal residual tumor at the bronchial resection margin. *Ann Thorac Surg* 1989;47:265–269.
12. Soorae AS, Stevenson HM. Survival with residual tumor on the bronchial margin after resection for bronchogenic carcinoma. *J Thorac Cardiovasc Surg* 1979;78:175–180.
13. Travis WD, Colby TV, Corrin B, et al. World Health Organization. International Histological Classification of Tumors: Histological Typing of Lung and Pleural Tumors, 3rd Ed. Heidelberg: Springer, 1999.
14. Asamura H, Naruke T, Tsuchiya R, et al. Bronchopleural fistulas associated with lung cancer operations. *J Thorac Cardiovasc Surg* 1992;104:1456–1464.

ELSEVIER

European Journal of Cardio-thoracic Surgery 34 (2008) 510–513

EUROPEAN JOURNAL OF CARDIO-THORACIC SURGERY

www.elsevier.com/locate/ejcts

Clinical application of costal coaptation pins made of hydroxyapatite and poly-L-lactide composite for posterolateral thoracotomy

Riken Kawachi, Shun-ichi Watanabe, Kenji Suzuki, Hisao Asamura *

Thoracic Surgery Division, National Cancer Center Hospital, 1-1 Tsukiji 5-chome, Chuo-ku, Tokyo 104-0045, Japan

Received 22 November 2007; received in revised form 7 May 2008; accepted 19 May 2008; Available online 2 July 2008

Abstract

Background: Costal coaptation pins made of hydroxyapatite and poly-L-lactide (HA/PLLA) composite are used to prevent slippage of the connected ribs in posterolateral thoracotomy. The objective of this study was to evaluate rib fixation achieved by HA/PLLA costal coaptation pins. **Methods:** Between September 2005 and January 2006, HA/PLLA costal coaptation pins were used in 106 consecutive patients who underwent posterolateral thoracotomy at the National Cancer Center Hospital, Tokyo, Japan. Among these, 96 patients who were followed for one year were analyzed. Fixation was assessed on chest X-ray at one week, two months, and one year after surgery, and classified into four types: no displacement, vertical displacement, lateral displacement, and combined vertical with lateral displacement. **Results:** The incidence of displacement at one week, two months, and one year after surgery was 22%, 19%, and 31%, respectively. No severe adverse events leading to the removal of HA/PLLA pins occurred. At one year, the most frequent type of displacement was vertical displacement (15%), which reflected a delay in bone formation. The use of analgesics among patients with different types of displacement was not significantly different ($p = 0.97$). **Conclusions:** Based on the results of this study, the fixation of cut ribs with HA/PLLA costal coaptation pins may be less advantageous in posterolateral thoracotomy, as displacement and delay of bone formation appear to occur frequently.

Keywords: Chest wall; Lung cancer; Pain; Tissue engineering; Thoracotomy

1. Introduction

A fixation device made of hydroxyapatite and poly-L-lactide (HA/PLLA) composite is a newly developed modality that is being increasingly used in thoracic surgery. Costal coaptation pins made of HA/PLLA are absorbable, easy to handle, and safe to use. Costal coaptation pins are used for rib fixation during posterolateral thoracotomy and to reposition multiple rib fractures [1–5]. There have been few reports on the use of HA/PLLA costal coaptation pins for thoracotomy, and in particular it has not been well documented whether such costal pins are beneficial for rib fixation. The objective of the present study was to evaluate post-thoracotomy rib displacement over time based on radiographic findings.

2. Materials and methods

2.1. Patients

Between September 2005 and January 2006, 135 lung resections were performed at the National Cancer Center Hospital, in Tokyo, Japan. Costal coaptation pins made of HA/PLLA composite were used in 106 consecutive patients who underwent posterolateral thoracotomy during the same period. Costal pins were not applied for the following reasons: wedge resection without rib resection in 12 patients, and complicated resection, such as chest wall resection, in 17 patients. The patient characteristics are shown in Table 1.

2.2. PLLA costal coaptation pins and the surgical procedure

Two sizes of HA/PLLA costal coaptation pins (Super-FIXSORB®: Ethicon Inc., Somerville, NJ) were used: 2 mm × 2 mm × 27 mm (thin) and 3 mm × 3 mm × 34 mm (thick) (Fig. 1). During posterolateral thoracotomy, the ribs were usually cut at the costal angle. The caliber was measured by a calibrator, and the bone marrow space was dilated using a reamer, if necessary. Small holes were made on both sides of the cut ribs using a drill. An absorbable suture

* Corresponding author. Address: Thoracic Surgery Division, National Cancer Center Hospital, 5-1-1 Tsukiji, Chuo-ku, Tokyo 104-0045, Japan.
Tel.: +81 3 3542 2511; fax: +81 3 3542 3815.
E-mail address: hasamura@ncc.go.jp (H. Asamura).

1010-7940/$ – see front matter
doi:10.1016/j.ejcts.2008.05.019

Table 1
Patient characteristics

Characteristic	(n = 106)
Age (years)	
Median	67
Range	31–84
Gender (%)	
Male	66 (62)
Female	40 (38)
Size of pins (%)	
Thin	56 (53)
Thick	50 (47)
Disease (%)	
Lung cancer	94 (89)
Others	12 (11)
Operative procedure (%)	
Limited resection	12 (11)
Lobectomy	88 (83)
Pneumonectomy	6 (6)

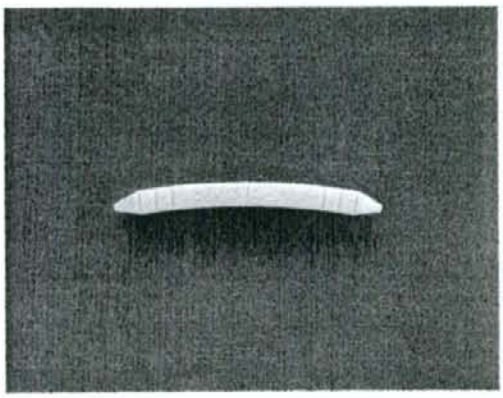

Fig. 1. Costal coaptation pins were used to close the posterolateral thoracotomy. The pin sizes were 2 mm × 2 mm × 27 mm (thin) and 3 mm × 3 mm × 34 mm (thick).

was threaded through the rib holes, and the pins were inserted into the bone marrow of the cut rib. The cut ribs were connected and ligated (Fig. 2).

2.3. Radiographic evaluation

Chest X-rays (posteroanterior view) were obtained at one week, two months, and one year after surgery. Based on the degree of fixation, the patients were classified into four groups: no displacement, vertical displacement, lateral displacement, and combined vertical with lateral displacement (Fig. 3). Displacement was defined as being vertical when the shift was more than one third of a rib's width, and as being lateral when the shift was ≥5 mm.

2.4. Statistical analysis

Statistical analyses were performed using SPSS software, version 13.0J (SPSS Inc., Chicago, IL). The chi-square test and

Fig. 2. A hand-drill was used to make holes on both sides of the cut rib (a). The caliber was measured by a calibrator, and a reamer was used to dilate the bone marrow space (b). Costal coaptation pins were inserted into the bone marrow (c). The ribs were ligated with absorbable sutures, and connected (d).

Mann–Whitney's *U*-test were used to determine the relationship between rib displacement and clinical factors. A *p*-value ≤0.05 was considered significant.

3. Results

3.1. Clinical findings

Of the 106 patients, 93 were followed for one year. In 13 patients, the follow-up was not complete: 9 patients had recurrence or died, and 4 patients were followed only with computed tomography. Displacement according to the

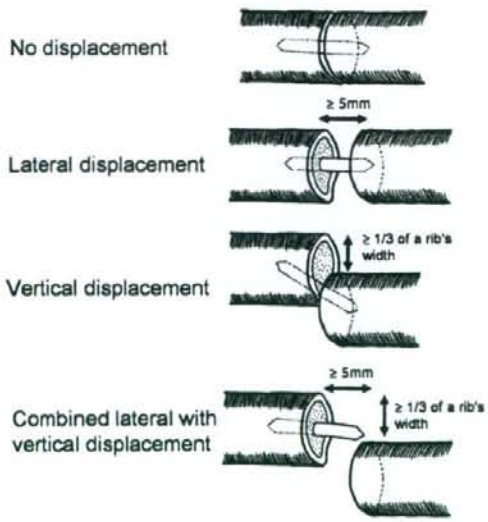

Fig. 3. The degree of fixation was categorized as no displacement, vertical displacement, lateral displacement, or combined vertical with lateral displacement.

Table 2
Displacement according to clinical and surgical factors

Character	Fixation			
	Displacement (−) (n = 64)	Displacement (+) (n = 29)	Total (n = 93)	p value
Age (years)				0.32
Median	70	63	67	
Range	31–80	50–84	31–84	
Gender (%)				0.78
Male	41 (71)	17 (29)	58	
Female	23 (66)	12 (34)	35	
Size of pins (%)				0.92
Thin	33 (67)	16 (33)	49	
Thick	31 (71)	13 (29)	44	
Disease (%)				0.99
Lung cancer	59 (69)	26 (31)	85	
Others	5 (63)	3 (37)	8	
Operative procedure (%)				0.45
Limited resection	6 (86)	1 (14)	7	
Lobectomy	56 (68)	27 (32)	82	
Pneumonectomy	2 (50)	2 (50)	4	
Analgesic intake at two months after surgery (%)				0.97
(−)	51 (69)	23 (31)	74	
(+)	13 (68)	6 (32)	19	

clinical and surgical factors of the 106 patients who were followed for one year is shown in Table 2.

3.2. Radiographic findings of displacement

The radiographic findings according to the type of displacement are shown in Table 3. The characteristic features were the incidence of displacement and the variation of displacement over time. Displacement occurred in 20 patients (22%) at one week, 18 patients (19%) at two months, and 29 patients (31%) at one year after surgery. Vertical displacement was more common during the early period after surgery, and lateral displacement was more frequent one year after surgery. Of the 73 patients who did not have displacement one week after surgery, 24 developed some displacement during follow-up; in 15 (63%), displacement was noted between one week and two months. In contrast, displacement improved in 12 patients between one week and two months.

One year after surgery, 12 patients had lateral displacement; in these patients, the chest X-ray showed a lucent zone at the connection of the ribs. In patients who had lateral displacement, computed tomography showed that the ribs were completely separated, and no bone tissue was observed (Fig. 4).

Table 3
Displacement over time

	Time after surgery		
	One week (%)	Two months (%)	One year (%)
No displacement	73 (78)	75 (81)	64 (69)
Vertical displacement	18 (19)	14 (15)	10 (11)
Lateral displacement	1 (1)	2 (2)	14 (15)
Combined displacement	1 (1)	2 (2)	5 (5)

3.3. Clinical findings and displacement

With respect to the results associated with different surgical procedures, 29 patients with rib displacement (32%) had lobectomy or pneumonectomy, and 1 patient had a limited resection (14%); the difference in rib displacement between surgical procedures was not significant ($p = 0.56$).

The effect of rib displacement on pain was assessed. Surgical wounds, which included the rib connection, were considered painful when oral analgesics were required two months after surgery. Nineteen patients were prescribed oral analgesics two months after surgery. Of these 19 patients, 13 had no displacement (20%), and 6 had displacement (21%); 2 patients had vertical displacement, 3 had lateral displace-

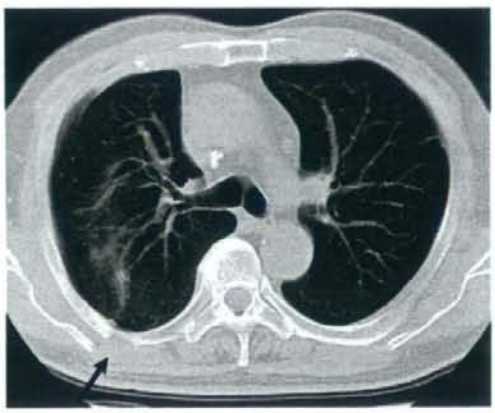

Fig. 4. The arrow shows the rib connection. The edge of the cut rib is clubbed, and the pin is not covered with bone tissue; a bare costal coaptation pin is present.

ment, and 1 had the combined type. Thus, there was no significant difference in analgesic use among the groups ($p = 0.97$). Moreover, complications (parenchymal lung injury and sputum retention with atelectasis) which induced excessive cough and subsequent costal dislocation were not seen in our series.

4. Comment

Absorbable fixation devices made of hydroxyapatite and poly-L-lactide (HA/PLLA) composite are increasingly being used in orthopedic surgery for procedures such as fractured bone fixation and bone grafting. In thoracic surgery, costal pins are used for fixation of the sternum and ribs in procedures for chest deformity, chest trauma, and thoracotomy. However, only a few reports have dealt with the use of costal coaptation pins [1–6]. The trend in thoracic surgery is toward a minimally invasive approach, and rib separation is not routinely performed, even in posterolateral thoracotomy in the present series, despite its widespread indication for intrathoracic diseases. When ribs are separated in thoracotomy, the need for rib coaptation has been controversial among thoracic surgeons, and the advantages of rib coaptation have not yet been defined [1,2]. The efficacy of coaptation pins has also not been adequately described. The present study focused on the use of HA/PLLA pins for the closure of posterolateral thoracotomy with regard to the incidence of displacement after surgery at the immediate, intermediate, and late postoperative periods.

The most remarkable finding of the present study was the high incidence of costal displacement even at the immediate postoperative period (one week after surgery) as high as 21%. Throughout the observation period, the incidence continued to be higher than 20%. In the literature, the incidence of displacement has been reported to be 2% by Tatsumi et al. and 1.3% by Tsunezuka et al. [1,2]. These reports concluded that PLLA costal coaptation pins were effective for the fixation of separated rib. Thus, there are large differences in the incidence of displacement between our study and these previous studies. The timing and method of postoperative evaluation might account for these differences. In the two previous studies, the timing of roentgenological evaluation varied, and chest CT was mainly used to evaluate displacement. For example, in Tatsumi's report, evaluation was performed with chest CT at 1–58 months after surgery [1]. The status of costal adaptation might be greatly influenced by the time after surgery, and the study should have incorporated a uniform timing for evaluation. Furthermore, the images on chest CT scan do not seem to be suitable for the evaluation of displacement in a vertical dimension. In fact, this method cannot detect displacement of less than 1 cm. Our strict criteria in the evaluation of displacement at scheduled timepoints could have detected even small displacement which might have been overlooked in previous studies.

Another important observation was the increase in the incidence of displacement during the follow-up period. The incidence varied from 21% at the immediate point to 31% at the late point postoperatively. The 21% incidence at the immediate postoperative period clearly indicated that fixation is not enough to ensure stability of the ribs. The increase in displacement at the late period might be caused by a decrease in the tension of the suture materials (absorbable strings). With regards to the ligation technique, ligation was performed with a single suture in our series. If double ligation had been made for tightening the cut rib, the rate of displacement might have decreased in the early period. The cut ribs were too small and too thin for double ligation, especially in the Japanese female patients. Regardless of the cause, the increased incidence in the late period, when bone coaptation should have been achieved, is a substantial problem in practice.

In this study, the status of rib displacement was classified into four patterns according to the images on postoperative chest X-rays. The most common pattern of displacement was lateral displacement (15%), followed by vertical displacement (11%), and combined lateral and vertical displacement (5%) at one year after surgery. On the other hand, two other reports did not show any differences in the incidence of displacement according to patterns [1,2]. The chest CT images of cases with lateral displacement in this series showed the complete separation of both costal ends and their bony clubbing. These findings suggested that bone formation around the costal pins was impaired. The costal pins could induce the proliferation of connective tissue around the pins, as reported previously, which results in impaired bone formation due to a foreign body reaction [7,8].

In summary, ribs connected with costal coaptation pins appear to deviate in a high percentage of patients, although the effect of such displacement on pain is likely minimal and no adverse events, such as parenchymal lung injury requiring reoperation to remove the pins, were noted. Rib fixation with HA/PLLA costal pins may be considered to be less advantageous in posterolateral thoracotomy.

References

[1] Tatsumi A, Kanemitsu N, Nakamura T, Shimizu Y. Bioabsorbable poly-L-lactide costal coaptation pins and their clinical application in thoracotomy. Ann Thorac Surg 1999;67(3):765–8.
[2] Tsunezuka Y, Iseki T, Sato H, Ishikawa N, Oda M, Watanabe G. A new technique of fixing a costal coaptation pin after resection of rib segment. Asian Cardiovasc Thorac Ann 2004;12(3):224–6.
[3] Iwasaki A, Hamatake D, Shirakusa T. Biosorbable poly-L-lactide rib-connecting pins may reduce acute pain after thoracotomy. Thorac Cardiovasc Surg 2004;52(1):49–53.
[4] Hirata T, Fukuse T, Mizuno H, Hitomi S, Wada H. Clinical application of biodegradable rib connecting pins in thoracotomy. Thorac Cardiovasc Surg 1999;47(3):183–7.
[5] Saito T, Iguchi A, Sakurai M, Tabayashi K. Biomechanical study of a poly-L-lactide (PLLA) sternal pin in sternal closure after cardiothoracic surgery. Ann Thorac Surg 2004;77(2):684–7.
[6] Lansman S, Serlo W, Linna O, Pohjonen T, Törmälä P, Waris T, Ashammakhi N. Treatment of pectus excavatum with bioabsorbable polylactide plates: preliminary results. J Pediatr Surg 2002;37(9):1281–6.
[7] Bergsma JE, de Bruijn WC, Rozema FR, Boering G, de Bruijn WC, Pennings AJ. Late degradation tissue response to poly(L-lactide) bone plates and screws. Biomaterials 1995;16(1):25–31.
[8] Bergsma EJ, Rozema FR, Bos RR, de Bruijn WC. Foreign body reactions to resorbable poly(L-lactide) bone plates and screws used for the fixation of unstable zygomatic fractures. J Oral Maxillofac Surg 1993;51(6):666–70.

Radiol Phys Technol (2008) 1:44–54
DOI 10.1007/s12194-007-0008-8

Experimental verification of proton beam monitoring in a human body by use of activity image of positron-emitting nuclei generated by nuclear fragmentation reaction

Teiji Nishio · Aya Miyatake · Kazumasa Inoue · Tomoko Gomi-Miyagishi · Ryosuke Kohno · Satoru Kameoka · Keiichi Nakagawa · Takashi Ogino

Received: 2 July 2007 / Revised: 22 October 2007 / Accepted: 23 October 2007 / Published online: 27 November 2007

Abstract Proton therapy is a form of radiotherapy that enables concentration of dose on a tumor by use of a scanned or modulated Bragg peak. Therefore, it is very important to evaluate the proton-irradiated volume accurately. The proton-irradiated volume can be confirmed by detection of pair-annihilation gamma rays from positron-emitting nuclei generated by the nuclear fragmentation reaction of the incident protons on target nuclei using a PET apparatus. The activity of the positron-emitting nuclei generated in a patient was measured with a PET-CT apparatus after proton beam irradiation of the patient. Activity measurement was performed in patients with tumors of the brain, head and neck, liver, lungs, and sacrum. The 3-D PET image obtained on the CT image showed the visual correspondence with the irradiation area of the proton beam. Moreover, it was confirmed that there were differences in the strength of activity from the PET-CT images obtained at each irradiation site. The values of activity obtained from both measurement and calculation based on the reaction cross section were compared, and it was confirmed that the intensity and the distribution of the activity changed with the start time of the PET imaging after proton beam irradiation. The clinical use of this information about the positron-emitting nuclei will be important for promoting proton treatment with higher accuracy in the future.

Keywords Proton therapy · Proton beam monitoring · Beam OFF-LINE PET system · PET-CT imaging

T. Nishio (✉) · T. Gomi-Miyagishi · R. Kohno · S. Kameoka · T. Ogino
Particle Therapy Division, Research Center for Innovative Oncology, National Cancer Center, Kashiwa,
6-5-1 Kashiwano-ha, Kashiwa-shi, Chiba 277-8577, Japan
e-mail: tnishio@east.ncc.go.jp

T. Nishio · A. Miyatake
Department of Nuclear Engineering and Management, Graduate School of Engineering, University of Tokyo,
2-11-16 Yayoi, Bunkyo-ku, Tokyo 113-0032, Japan

T. Nishio · K. Nakagawa
Department of Radiology, Graduate School of Medicine, University of Tokyo, 7-3-1 Hongo, Bunkyo-ku,
Tokyo 113-8655, Japan

K. Inoue
Department of Radiology, National Cancer Center, Kashiwa,
6-5-1 Kashiwano-ha, Kashiwa-shi, Chiba 277-8577, Japan

Present Address:
K. Inoue
Functional Imaging Division, Research Center for Innovative Oncology, National Cancer Center, Kashiwa,
6-5-1 Kashiwano-ha, Kashiwa-shi, Chiba 277-8577, Japan

K. Inoue
Graduate School of Health Science, Tokyo Metropolitan University, 7-2-10 Higashiogu, Arakawa-ku,
Tokyo 116-8551, Japan

1 Introduction

Proton therapy has allowed the dose to be concentrated only on a tumor. The use of proton therapy is spreading throughout the world as a highly accurate method of radiation therapy [1]. In the future, proton therapy will be expected to become one of the main forms of radiation therapy because of its high utility. On the other hand, the diagnosis of an initial or small tumor has become

possible with developments in imaging methods that provide high resolution and contrast. In particular, positron emission tomography (PET) has advanced rapidly, and its use has become widespread. PET-computed tomography (CT) combines PET and CT and is now readily available. The fusion of PET and CT images can be achieved with high precision by use of a PET-CT apparatus. As a result, the location of activity can be determined with high accuracy.

In this study, the activity of positron-emitting nuclei generated by the nuclear fragmentation reaction of incident protons and nuclei constituting of a patient body was measured with a PET-CT apparatus (beam OFF-LINE PET system), and the proton-irradiated volume was confirmed. So far most researches were limited to phantom studies using a PET apparatus (no combined with CT apparatus) [2–13]. Verification of activity measurement was performed in patients with tumors of the brain, head and neck, liver, lungs, and sacrum. By use of a fusion imaging obtained with a combined PET-CT apparatus, the irradiated volume was confirmed immediately after proton therapy with higher accuracy than that the use of fusion of images obtained from the separate PET apparatus and CT apparatus.

We are researching dose-volume delivery-guided proton therapy (DGPT) for confirmation of the proton-irradiated volume and dose distribution by using a beam ON-LINE PET system (BOLPs) in the proton treatment room [13]. The activity image of each treatment site obtained with the PET-CT apparatus will be used for the simulation and estimation of the activity image acquired from the BOLPs immediately after proton irradiation to a patient.

This paper is organized as follows. Experimental procedures are described in Sect. 2. Measurement and analysis results and discussion are presented in Sect. 3. Section 4 discusses the conclusions of this study regarding proton therapy.

2 Materials and methods

2.1 Nuclear fragmentation reaction of incident protons and target nuclei

The nuclear fragmentation reaction occurs in the human body by high-energy proton beam irradiation during proton therapy. Many kinds of nuclei, including positron-emitting nuclei, are generated by the reaction.

The activity $N_{\beta+}$ of the positron-emitting nuclei Y generated from each type of tissue composition by the nuclear fragmentation reaction is expressed as the following equation [11]:

$$\begin{aligned} &N_{\beta+}(tissue;E_p)\,[\mathrm{kBq/cc/GyE}] \\ &= \Phi_p(tissue;E_p) \\ &\cdot \sum_X \sum_Y \left| \begin{array}{l} \dfrac{1}{T_m}\cdot\left\{1-\exp\left(-\sigma_{X\to Y}(E_p)\cdot n_{tissue}(X)\cdot\Delta_{tissue}\right)\right\} \\ \times\left\{\dfrac{T_{1/2}(Y)}{T_i\cdot\ln 2}\cdot\left(1-2^{-T_i/T_{1/2}}(Y)\right)\right\} \\ \times 2^{-T_0/T_{1/2}}(Y)\times\left(1-2^{-T_m/T_{1/2}}(Y)\right) \end{array} \right| . \end{aligned} \tag{1}$$

Here, X denotes the target nuclei in the tissue, z the depth, T_m the time of the activity measurement, T_i the time of the proton irradiation, T_0 the interval between the start of the activity measurement and the discontinuation of proton irradiation, and $T_{1/2}$ the half life of the generated positron-emitting nuclei. The reaction cross section of $\sigma_{X\to Y}$, which determines the rate of generation in the nuclear fragmentation reaction $X(p,x)Y$, depends on the kind of target nucleus (mass number A_t, atomic number Z_t) and the relative kinetic energy of E_p. n_{tissue} denotes the number per unit volume of the nucleus in the tissue, and Δ_{tissue} the target thickness. Data of human body composition are based on ICRU Report 46 [14]. The number of incident protons per the dose and the volume Φ_p, is expressed as follows:

$$\begin{aligned} &\Phi_p(tissue;E_p)\,[\mathrm{protons/cc/GyE}] \\ &= 1\times10^{-3}\Big/\left\{\left(dE_p/_{dx}[\mathrm{J/cm}]\right)\cdot RBE\right\} \\ &= \left[1.671\times10^{-11}\cdot\left\{\frac{\ln\left(1.363\times10^4\cdot\left(\gamma(E_p)^2-1\right)\right)}{\beta(E_p)^2}-1\right\}\right]^{-1}. \end{aligned} \tag{2}$$

Here, RBE is the relative biological effectiveness. β and γ are expressed by use of the kinetic energy of the proton, in the following equation:

$$\begin{aligned} &\beta(E_p)=\sqrt{1-\frac{1}{\left(1+1.066\times10^{-3}\cdot E_p\right)^2}}, \\ &\gamma(E_p)=1+1.066\times10^{-3}\cdot E_p. \end{aligned} \tag{3}$$

The ^{12}C, ^{14}N, ^{16}O, and ^{40}Ca nuclei are main chemical elements of the human body [14]. For proton therapy, the number of each positron-emitting nuclei, generated in the human body depends on the target nuclei and on the incident proton beam energy.

Some the experimental data of the reaction for $^{12}C(p,x)Y$, $^{14}N(p,x)Y$, $^{16}O(p,x)Y$ have been reported [15]. The mean values of the reaction cross sections of the ^{11}C, ^{13}N, and ^{15}O nuclei generated from the ^{12}C and ^{16}O nuclei are especially expressed as follows [11]:

$$\sigma_{X\to Y}(E_p) = \frac{a}{1+\exp\left(\frac{b-E_p}{c}\right)} \cdot \left\{1 - d\cdot\left(1 - e\cdot\exp\left(-\frac{E_p - f}{g}\right)\right)^h\right\},$$

$$\begin{array}{cccccccccc} X & Y & a & b & c & d & e & f & g & h \\ \left[{}^{12}\mathrm{C}\right. & {}^{11}\mathrm{C} & 96.0 & 21.4 & 0.9 & 0.5 & 1.2 & 39.0 & 34.5 & 2.0\left.\right] \\ \left[{}^{16}\mathrm{O}\right. & {}^{15}\mathrm{O} & 71.0 & 26.0 & 2.8 & 0.6 & 1.1 & 41.0 & 36.0 & 6.0\left.\right] \\ \left[{}^{16}\mathrm{O}\right. & {}^{13}\mathrm{N} & 66.0 & 10.4 & 0.4 & 0.9 & 0.8 & 11.6 & 6.8 & 1.0\left.\right] \\ \left[{}^{16}\mathrm{O}\right. & {}^{11}\mathrm{C} & 18.8 & 43.6 & 3.6 & 0.5 & 1.0 & 49.0 & 35.0 & 4.0\left.\right] \end{array} \quad (4)$$

Here, the reaction cross section of $\sigma_{X\to Y}$ and the relative kinetic energy E_p have units of mb and MeV, respectively. The letters a, ..., h are constant parameters for the calculation of the reaction cross section in each reaction channel. The data of the reaction for $^{40}\mathrm{Ca}(p,x)Y$ is mainly calculated with the INTENSITY code [16, 17] because there is no experiment value.

2.2 Proton therapy at each treatment site

The proton radiotherapy facility of the National Cancer Center, Kashiwa has a small normal-conducting AVF cyclotron (C235) for medical purposes, two rotating gantry ports, and one horizontal fixed port [18, 19]. For obtaining laterally uniform irradiation fields, the dual-ring double scattering method is used in one rotating gantry port and the horizontal fixed port; the wobbler method is used with the other rotating port. The uniform proton dose distribution during proton treatment is controlled by a simple feed back control system equipped with an automatic fine adjustment of the beam axis and a mechanism for moving the second dual-ring scatter of the double scatters to the optimal position [20]. Using this system, we achieved uniform dose distribution in the irradiation field during proton radiotherapy, with symmetry within ±1% and flatness within 2%. The accuracy of the calculated dose is similarly proportional to the accuracy of the measured and calculated activities.

Verification of the activity measurement was performed in about 20 cases with tumors of the brain, head and neck, liver, lungs, and sacrum. Proton beam irradiation to the liver and lung was performed with synchronization to the respiratory motion of the target organ. The position uncertainty of the target organ is within 5 mm. The proton treatment planning system, PTPLAN/ndose, developed in our facility [21] was used for planning of the proton treatment. The accuracy of the proton range is estimated within 3 mm in conversion of Hounsfield units (HU) of the planning CT image to water equivalent length. The accuracy of the dose calculation will be within 5% for the homogeneous or simply inhomogeneous body (e.g., prostate, liver, lung), and be greater than 10% at the boundary of the inhomogeneous tissue (e.g., head and neck). The dose calculation was performed with the margin of the 3 mm for the brain and the head and neck, and 5 mm for the liver, the lung, and the prostate.

2.3 Measurement of activity with PET-CT apparatus

The activity of the positron-emitting nuclei generated in the patients by proton beam irradiation was measured with the PET-CT apparatus (Discovery ST (GE Medical Systems, Milwaukee, Wisconsin, U.S.A.)) at our institution. The PET-CT apparatus was a detection system with 10,080 BGO (Bismuth-Germanium-Oxide) with a crystal size of 6.2 × 6.2 × 30 mm^3 arranged on a circumference of a circle with a diameter of 88.6 cm. 3D reconstruction algorithm of OSEM (Ordered Subsets Expectation Maximization) was employed with a position resolution of 5.0–6.7 mm, which was position-dependent. The axial size of the field of view (FOV) was 15.7 cm. The accuracy of the absolute activity measured with the commercial PET-CT apparatus has been reported to be commonly about 10% [22].

The distance between the room for proton treatment and the room with the PET-CT apparatus was about 40 m. Therefore, PET scanning was started about 7 min after irradiation, and the image was acquired over 5 min. Therefore, the biological washout effect in the metabolism of a living tissue is important for the verification of the absolute activity and the activity distribution of the positron-emitting nuclei induced by the proton irradiation. In studies in which the radioactive ion beam ($^{11}\mathrm{C}$,$^{10}\mathrm{C}$) to a rabbit was irradiated, the decay curve has three components of a fast decay (decay constant ~2–10 s), medium decay (decay constant ~100–200 s), and slow decay (decay constant ~3,000–10,000 s) [23, 24]. The 50–65% of total activity is the fast and medium components.

The proton beam was irradiated to the tumor in the liver and lungs with the beam synchronized to respiratory motion. However, the activity of the positron-emitting nuclei generated in the patient was measured without synchronizing to respiratory motion of the target organ. The corresponding tumor movement will be a few cm.

3 Results and discussion

3.1 Visual verification of PET-CT image at each treatment site

The measured activity distribution and the calculated dose distribution on CT image for proton treatment of a tumor in the sacrum as one of the site studies are shown in Fig. 1. Proton beam irradiation was performed with a gantry angle of 180 degrees and a dose of 2.5 GyE [= [Gy] x *RBE* (= 1.1 = constant)]. Moreover, the width of the spread-out Bragg peak (SOBP) was 70 mm. The activity fitted on the area of proton irradiation was visually confirmed by comparison with the proton dose distribution. The activity observed in the proton irradiated area of subcutaneous adipose tissue and bone tissue was higher than that in the surrounding area.

Figure 2 shows the results for prostate tumor. Proton beam irradiation was performed with a gantry angle of 90°, a SOBP width of 60 mm, and a dose of 2.0 GyE. Similarly, high activity was observed in the subcutaneous adipose tissue and in the femur.

Figure 3 shows the results for a tumor of the head and neck. Proton beam irradiation was performed twice with each dose of 2.0-GyE, and a gantry angle of 230° for the initial exposure, followed by 330° for the second one. The respective widths of the SOBP were 80 and 70 mm. The interval between the two irradiation procedures was about 9 min. Therefore, the activity of the 330° proton beam was higher than that of the 230° beam. High activity was similarly observed in the areas of adipose tissue and maxilla irradiated by the proton beam.

Figure 4 shows the results for a liver tumor. Proton beam irradiation was performed with a 3.8-GyE dose and 80 mm SOBP from a gantry angle of 290°. During treatment, the proton beam irradiation was synchronized to the respiratory motion of the target organ. However, during the acquisition of PET-CT image data, there was no synchronization to the respiratory motion. Similarly, high activity was observed in the area of subcutaneous adipose tissue. The findings of activity during proton treatment after a transarterial chemoembolization therapy (TACE) procedure using lipiodol for a liver tumor are shown in Fig. 5. The CT value of 80–350 HU in area including the lipiodol is considerably higher than 70 HU in a normal liver. Proton beam irradiation was performed with a 3.8-GyE dose and 80 mm SOBP at a gantry angle of 180°. The activity in the liver tumor was high. We speculated that this was because many positron-emitting nuclei were generated from the iodine nuclei contained in the lipiodol.

3.2 Specificity of activity generated in each body tissue

The activity in each tissue and the interval between beam-stop time and start-time of activity measurement was calculated from Eq. 1. A beam irradiation time of 2 min and the beam energy in each tissue are used in the calculation. The reaction cross sections of $^{12}C(p,x)^{11}C$, $^{16}O(p,x)^{15}O$, $^{16}O(p,x)^{13}N$, and $^{16}O(p,x)^{11}C$ reactions were calculated from Eq. 4 at each proton energy. The reaction cross sections of $^{12}C(p,x)^{10}C$, $^{16}O(p,x)^{14}O$, $^{40}Ca(p,x)^{38}K$, $^{40}Ca(p,x)^{30}P$, $^{40}Ca(p,x)^{15}O$, $^{40}Ca(p,x)^{13}N$, and $^{40}Ca(p,x)^{11}C$ reactions were calculated with the INTENSITY code. For

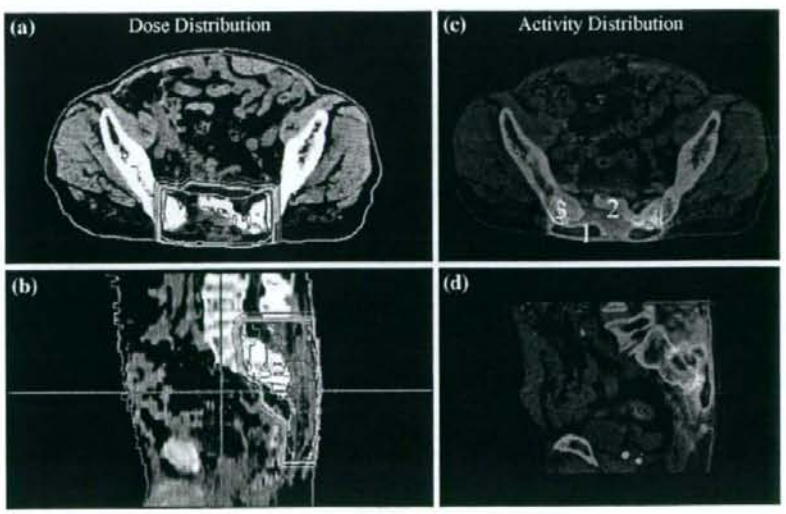

Fig. 1 Dose distribution calculated with the proton treatment planning system and activity measured with the PET-CT apparatus on CT image after proton treatment of tumor in the sacrum. The iso-dose line of 100% is red, 80% yellow green, 50% light blue, and 20% purple. The activity line of 5 kBq/cc is red, 3 kBq/cc green, and 1 kBq/cc bule. Proton beam irradiation was performed with an SOBP of 70 mm, gantry angle of 180°, and dose of 2.5 GyE. The dose distributions on each CT image in axial and coronal planes are shown in figures (**a**) and (**b**), and the activity are shown in figures (**c**) and (**d**)

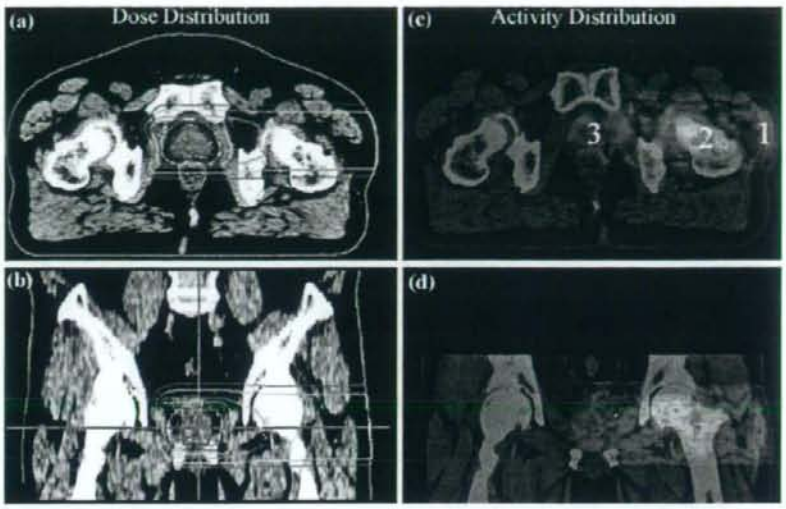

Fig. 2 Dose distribution calculated with the proton treatment planning system and activity measured with the PET-CT apparatus on CT image after proton treatment of tumor in the prostate. The iso-dose line of 100% is red, 80% yellow green, 50% light blue, and 20% purple. The activity line of 5 kBq/cc is red, 3 kBq/cc green, and 1 kBq/cc bule. Proton beam irradiation was performed with an SOBP of 60 mm, gantry angle of 90°, and dose of 2.0 GyE. The dose distributions on each CT image in axial and coronal planes are shown in figures (**a**) and (**b**), and the activity are shown in figures (**c**) and (**d**)

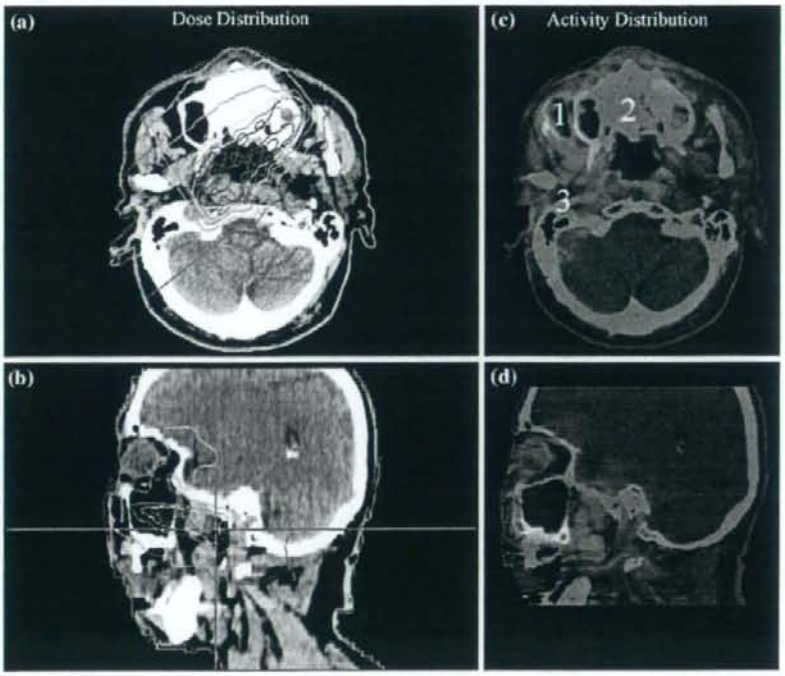

Fig. 3 Dose distribution calculated with the proton treatment planning system and activity measured with the PET-CT apparatus on CT image after proton treatment of tumor in the head and neck. The iso-dose line of 100% is red, 80% yellow green, 50% light blue, and 20% purple. The activity line of 5 kBq/cc is red, 3 kBq/cc green, and 1 kBq/cc bule. Proton beam irradiation was performed with an SOBP of 70 mm, gantry angle of 330°, and dose of 2.0 GyE after irradiation with an SOBP of 80 mm, gantry angle of 230°, and dose of 2.0 GyE. The dose distributions on each CT image in axial and coronal planes are shown in figures (**a**) and (**b**), and the activity are shown in figures (**c**) and (**d**)

$^{14}N(p,x)^{13}N$, $^{14}N(p,x)^{11}C$, and $^{14}N(p,x)^{10}C$ reactions, experimental data [15] were used. The results are shown in Fig. 6. Data of each human body composition and the proton energy used for the calculation of the time dependent activity in various tissues are shown in Table 1. The activity of adipose tissue was higher than that in the liver more than 6 min after proton beam irradiation. The same tendency was shown for activity measurements with use of the PET-CT apparatus after proton treatment for liver cancer.

The calculated decay curve is approximated with two components of short (^{15}O, ^{14}O, ...) and long (^{13}N, ^{11}C, ...) half life, and is expressed as the following equation:

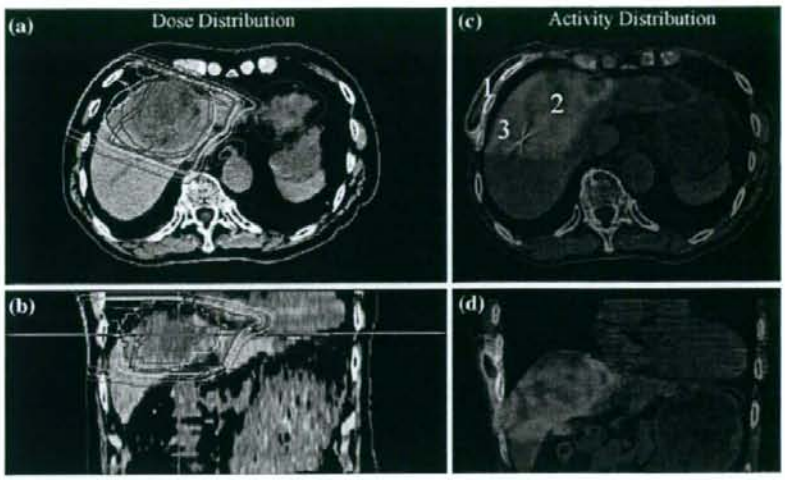

Fig. 4 Dose distribution calculated with the proton treatment planning system and activity measured with the PET-CT apparatus on CT image after proton treatment of tumor in the liver. The iso-dose line of 100% is red, 80% yellow green, 50% light blue, and 20% purple. The activity line of 7 kBq/cc is red, 5 kBq/cc green, and 3 kBq/cc bule. The proton beam irradiation was performed with an SOBP of 80 mm, gantry angle of 290°, and dose of 3.8 GyE. The dose distributions on each CT image in axial and coronal planes are shown in figures (**a**) and (**b**), and the activity are shown in figures (**c**) and (**d**)

$$N_{\beta+}(Tissue;T_0)[\mathrm{kBq/cc/GyE}] = \begin{cases} 2.2\times 2^{-T_0[\mathrm{min}]/1.9}+0.6\times 2^{-T_0[\mathrm{min}]/17.7} & (\mathrm{Tumor}) \\ 3.1\times 2^{-T_0[\mathrm{min}]/2.0}+0.5\times 2^{-T_0[\mathrm{min}]/16.8} & (\mathrm{Liver}) \\ 1.4\times 2^{-T_0[\mathrm{min}]/1.9}+0.8\times 2^{-T_0[\mathrm{min}]/18.6} & (\mathrm{Adipose\ Tissue}) \\ 5.9\times 2^{-T_0[\mathrm{min}]/2.0}+1.6\times 2^{-T_0[\mathrm{min}]/17.8} & (\mathrm{Skeleton\ Cranium}) \\ 3.0\times 2^{-T_0[\mathrm{min}]/1.9}+1.4\times 2^{-T_0[\mathrm{min}]/17.8} & (\mathrm{Skeleton\ Femur}) \\ 4.3\times 2^{-T_0[\mathrm{min}]/1.9}+1.3\times 2^{-T_0[\mathrm{min}]/17.4} & (\mathrm{Skeleton\ Ribs}) \end{cases} \quad (5)$$

The value of short or long half life in each tissues was consistent within 5% accuracy, and was equal to the our study using a dead rabbit [13]. This result showed that the activity at $T_0 = 0$ (condition of the measurement in the BOLPs) was higher five times than that at $T_0 = 7$ min (condition of this work in the commercial PET-CT apparatus).

Figure 7 shows the ratio R of the calculated activity normalized to one at $T_0 = 0$. It is expressed as the following equation:

$$R(tissue;T_0) = \frac{N_{\beta+}(Tumor;T_0=0)}{N_{\beta+}(Tissue;T_0=0)} \cdot \frac{N_{\beta+}(Tissue;T_0)}{N_{\beta+}(Tumor;T_0)}. \quad (6)$$

The results showed that the image of the activity changed during $T_0 = 0 \sim 10$ min. Therefore, the observed image of off-line PET (commercial PET-CT apparatus) will be different from that of the on-line PET (BOLPs).

The value of the activity at points 1, 2, and 3 on the axial activity images are shown in Figs. 1, 2, 3, 4 and 5. The points were selected on the soft tissue (tumor), the subcutaneous adipose tissue, and the bone tissue. The reaction cross sections, the kinetic energies of the proton beam at each point, and the half lives of the positron-emitting nuclei are shown in Table 2. The irradiation dose, irradiation time, interval between discontinuing the beam and acquiring the PET image, and the measured, the calculated value (Calculation: B) and the differences of activity at the point are summarized in Table 3.

It was estimated that the measured activity had a statistical accuracy of 9% (2 kBq/cc at 10 cm path length in the human body, 5 min measurement, each cubic voxel with a perimeter of 4 mm), and the image reconstruction accuracy was 10%. The accuracy of the measured activity in the biological washout effect is estimated to be very large, and is difficult to show the correspondence quantitatively. Moreover, the coefficient of the effect is always smaller than one. In the calculated activity, the accuracy of the reaction cross sections and the number of incident protons were estimated to be 20 and 5%, respectively. In the soft tissue and the liver, the measurement and the calculation activity were consistent within the error bar. On the other hand, the measured activity was about two to four times as large as the calculated activity in the adipose tissue, and about two times that in the femur. In the high activity of the adipose tissue, the accuracy of the attenuation correction factor of the 511-keV gamma ray based on the CT value of the subcutaneous adipose tissue under the adjacent body surface will partly influence the discrepancy in the activity measurement. The high activity of the femur was probably due to the accuracy of the calculation based on the fragmentation reaction cross section of ^{40}Ca. In the liver tumor after a TACE procedure with lipiodol, the measured activity was about four times as large as the calculated activity in the case without the lipiodol. It is noted that the nuclear fragmentation reaction of the iodine contained in the lipiodol is unknown well.

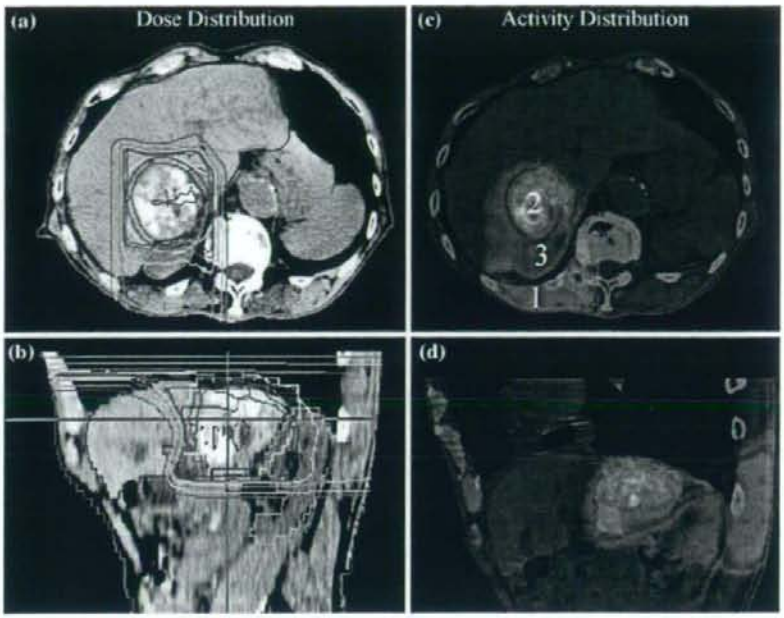

Fig. 5 Dose distribution calculated with the proton treatment planning system and activity measured with the PET-CT apparatus on CT image after proton treatment of liver tumor following TACE. The iso-dose line of 100% is red, 80% yellow green, 50% light blue, and 20% purple. The activity line of 7 kBq/cc is red, 5 kBq/cc green, and 3 kBq/cc bule. Proton beam irradiation was performed with an SOBP of 80 mm, gantry angle of 180 degrees and dose of 3.8 GyE. The dose distributions on each CT image in axial and coronal planes are shown in figures (**a**) and (**b**), and the activity are shown in figures (**c**) and (**d**)

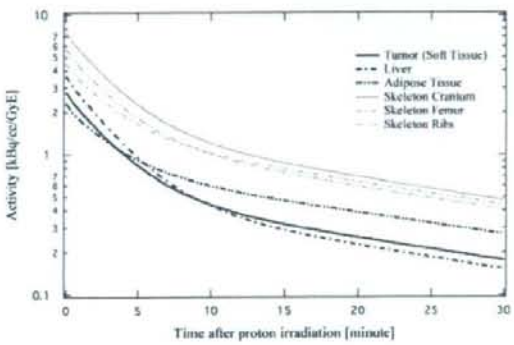

Fig. 6 Calculated activity $N_{\beta+}$ to the interval between the stopping beam and starting measurement of the activity in various tissues

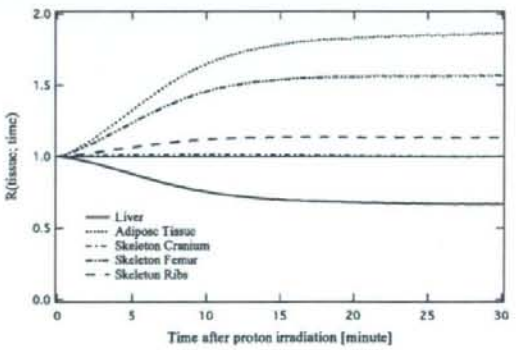

Fig. 7 Ratio R of the calculated activity normalized to one at $T_0 = 0$ in various tissues

Table 1 Data of human body composition and proton energy used for the calculation of the time dependent activity in various tissues

Body tissue	n_{tissue} (X)(10^{22}/cm^3)					Proton energy (MeV)
	H	C	N	O	Other (Ca)	
Tumor (soft tissue)	6.6	1.3	0.1	2.4	0.0	60.4
Liver	6.6	0.7	0.1	2.9	0.0	70.6
Adipose tissue	6.6	2.5	0.1	1.3	0.0	114.3
Skeleton cranium	5.9	2.1	0.3	3.2	0.3	89.1
Skeleton femur	6.4	2.6	0.2	2.1	0.1	141.6
Skeleton ribs	6.3	2.1	0.3	2.7	0.2	109.6

"Calculation: C" in Table 3 is the calculated activity in the simulation of the 5 min measurement with a PET apparatus immediately after the proton irradiation. As a result, it was estimated that the activity was about 10 kBq/cc per 2.5-GyE dose immediately after the proton irradiation.

The biological washout effect will greatly affect the accuracy of the measured activity. The coefficient of the effect has been estimated to be the 50–65% of total activity [23, 24]. However, the radioactive ion beam was irradiated to a living tissue in the study. A flow-out of the positron-emitting nuclei implanted by the radioactive ion

Table 2 Proton energy, reaction cross section, half life used for the calculation of the activity in human body

Treatment site	Interest point	Proton energy (MeV)	Irradiation dose (GyE)	Cross section (mb)														
				Target nuclei	^{12}C	^{12}C	^{14}N	^{14}N	^{14}N	^{16}O	^{16}O	^{16}O	^{16}O	^{16}O	^{40}Ca	^{40}Ca	^{40}Ca	^{40}Ca	^{40}Ca
				PositronEmitting nuclei	^{11}C	^{10}C	^{13}N	^{11}C	^{10}C	^{15}O	^{14}O	^{13}N	^{11}C	^{10}C	^{38}K	^{30}P	^{15}O	^{13}N	^{11}C
				Half life (min)	20.39	0.321	9.965	20.39	0.321	2.037	1.177	9.965	20.39	0.321	7. 636	2.498	2.037	9.965	20.39
Sacrum	1	73.1	2.5		81.3	4.4	16.1	52.4	6.5	69.8	1.7	6.6	18.2	1.8	14.1	9.2	2.2	2.2	2.2
	2	48.4	2.5		95.6	5.2	24.1	65.3	8.0	71.0	1.7	6.8	14.9	1.9	14.1	9.2	2.2	2.2	2.2
	3	62.1	2.5		88.9	4.8	6.6	18.6	1.9	70.9	1.7	6.6	18.6	1.9	14.1	9.2	2.2	2.2	2.2
Prostate	1	173.0	1.4		50.3	2.7	8.1	13.7	1.7	35.1	0.8	6.6	10.4	0.9	14.1	9.2	2.2	2.2	2.2
	2	137.7	1.4		54.4	2.9	14.9	11.6	1.4	44.3	1.1	6.6	12.1	1.2	14.1	9.2	2.2	2.2	2.2
	3	63.3	2.0		88.1	4.8	19.0	58.6	7.2	70.8	1.7	6.6	18.6	1.9	14.1	9.2	2.2	2.2	2.2
Head and neck	1	103.3	2.7		64.2	3.5	12.3	33.3	4.1	59.4	1.4	6.6	15.2	1.6	14.1	9.2	2.2	2.2	2.2
	2	70.4	3.7		83.2	4.5	16.9	54.1	6.7	70.2	1.7	6.6	18.4	1.9	14.1	9.2	2.2	2.2	2.2
	3	115.9	1.7		59.6	3.2	13.2	25.4	3.1	53.4	1.3	6.6	13.8	1.4	14.1	9.2	2.2	2.2	2.2
Liver	1	121.1	3.2		58.1	3.1	13.6	22.1	2.7	51.1	1.2	6.6	13.4	1.3	14.1	9.2	2.2	2.2	2.2
	2	75.9	3.8		79.4	4.3	15.2	50.6	6.2	69.3	1.6	6.6	18.0	1.8	14.1	9.2	2.2	2.2	2.2
	3	100.8	3.8		65.3	3.5	12.1	34.9	4.3	60.6	1.4	6.6	15.5	1.6	14.1	9.2	2.2	2.2	2.2
Liver	1	131.9	3.1		55.5	3.0	14.5	15.3	1.9	46.5	1.1	6.6	12.5	1.2	14.1	9.2	2.2	2.2	2.2
	2	71.8	3.8		82.2	4.4	16.5	53.2	6.6	70.0	1.7	6.6	18.3	1.8	14.1	9.2	2.2	2.2	2.2
	3	110.0	3.4		61.6	3.3	12.8	29.1	3.6	56.2	1.3	6.6	14.5	1.5	14.1	9.2	2.2	2.2	2.2

beam is the washout effect. On the other hand, in our study, the positron-emitting nuclei are generated from the nuclei in a tissue constituting a human body. Therefore, physiology, the effect has a different possibility. Perhaps, it is guessed that the effect may be not too large at our study.

The measured and calculated activities summarized in Table 3 will have the large error bar of a few 10%, and be scarcely correspondent within the large error bar in the soft tissue and the bone tissue except a skeleton femur. The measured activities in the subcutaneous adipose tissue, the skeleton femur, and the liver tumor after a TACE procedure are about two to three times higher than the calculated activities. Anyway the reason of large disagreement is not clear.

3.3 Comparison between proton dose distribution and activity distribution

The activity distribution visually corresponded to the proton dose distribution in Figs. 1, 2, 3, 4 and 5. Figure 8 shows the dose and activity distributions with a spike shape on the sagittal CT image in the head and neck. The position of the dose and activity distributions of the spike shape was consistent. However, it is difficult to show the correspondence quantitatively. We have executed the quantitative evaluation concerning the correspondence of the proton dose distribution and the activity distribution by our previous research [11, 13]. As the results, the activity range was about 7 mm shorter in a water equivalent length than the proton range expected from the energy threshold for the

Table 3 Proton irradiation dose, irradiation time, time of activity measurement, and level of activity measured and calculated

Treatment site	Irradiation dose (GyE/fx.)	Irradiation time (s)	Interval between stopping beam and starting measurment (s)	Point	Irradiation dose (GyE)	Activity (kBq/cc)		A/B	Activity (kBq/cc) Calculation:C
						Measurement:A	Calculation:B		
Sacrum	2.5	55	430	1	2.5	3.8(± 0.5)	1.7(± 0.4)	2.2(± 0.6)	5.5(± 1.2)
				2	2.5	1.8(± 0.2)	2.1(± 0.4)	0.9(± 0.5)	8.5(± 1.8)
				3	2.5	2.5(± 0.3)	2.5(± 0.5)	1.0(± 0.6)	10.2(± 2.1)
Prostate	2.0	41	450	1	1.4	4.6(± 0.6)	1.1(± 0.2)	4.2(± 0.7)	3.3(± 0.7)
				2	1.4	4.2(± 0.6)	1.8(± 0.4)	2.3(± 0.7)	6.7(± 1.4)
				3	2.0	1.2(± 0.2)	1.3(± 0.3)	0.9(± 0.3)	6.1(± 1.3)
Head and neck	4.0	45	436	1	2.7	4.4(± 0.6)	1.7(± 0.4)	2.6(± 0.7)	3.0(± 0.6)
				2	3.7	3.0(± 0.4)	4.1(± 0.9)	0.7(± 0.9)	25.1(± 5.2)
				3	1.7	1.1(± 0.1)	1.4(± 0.3)	0.8(± 0.3)	13.1(± 2.7)
Liver	3.8	108	390	1	3.2	7.5(± 1.0)	2.4(± 0.5)	3.1(± 1.1)	6.5(± 1.4)
				2	3.8	2.3(± 0.3)	2.6(± 0.5)	0.9(± 0.6)	12.8(± 2.7)
				3	3.8	2.6(± 0.3)	2.8(± 0.6)	0.9(± 0.7)	13.6(± 2.8)
Liver	3.8	158	505	1	3.1	3.6(± 0.5)	2.0(± 0.4)	1.8(± 0.6)	5.8(± 1.2)
				2	3.8	6.9(± 0.9)	1.8(± 0.4)	3.8(± 1.0)	11.0(± 2.3)
				3	3.4	2.3(± 0.3)	1.8(± 0.5)	1.2(± 0.5)	11.1(± 2.3)

Fig. 8 Dose distribution and activity distribution on CT image after proton treatment of tumor in the head and neck. The *arrow* indicates the dose point of the spike shape

nuclear fragmentation reaction in a mono-energetic proton beam. Moreover, it was confirmed that the lateral activity distribution corresponds to the real beam size with an accuracy within 1 mm. In the therapeutic SOBP proton beam, the difference of the range between proton beam and the activity is larger than the case of a mono-energetic proton beam. Moreover, the therapeutic SOBP beam deteriorates the correspondence between the lateral dose and the activity distributions.

There is no simple relation between the stopping power of proton beam that determines the proton dose distribution and the cross section of the nuclear fragmentation reaction expressed as Eq. 1. Therefore, the activity distribution has no sharp peak like the Bragg peak in the proton dose distribution. For a proton therapy, it is very large impact to monitor the therapeutic proton dose distribution by use of the activity distribution in a patient. Therefore, it is necessary to innovatively research the physical reaction mechanism of the nuclear fragmentation reaction.

In the position of the proton-irradiated volume in the patient, the accuracy at the lateral dose and activity distributions will be about half cm, and the accuracy at the distal distributions cm order by the effects of the energy threshold for the nuclear fragmentation reaction and the SOBP width in the target organ without the respiratory motion (head and neck, etc). On the other hand, the accuracy at the lateral dose and activity distributions will be a few cm on the direction of the organ motion especially in the target organ with the respiratory motion (liver, etc) for the PET measurement without synchronization. In a proton treatment planning at our facility, planning target volume (PTV) has the margin of 3–10 mm in clinical target volume (CTV) by each treatment site. It will be visually confirmed whether gross tumor volume (GTV) is inside the proton-irradiated field.

4 Conclusion

In proton therapy, the proton-irradiated volume in the patient body was visually confirmed by measurement of the activity of the positron-emitting nuclei generated by the nuclear fragmentation reaction by use of the PET-CT apparatus. Moreover, verifications of the distribution and intensity of activity were performed for each body tissue composition. As yet, quantitative evaluations of the absolute activities remain.

To date, the acquisitions of PET and CT images were executed separately by use of each apparatus [7, 9]. There was a limit on the precision of image fusion. Therefore, determining whether the activity in the ribs or subcutaneous adipose tissue was high was previously very difficult after proton treatment of liver and lung cancers [7]. In this study, the confirmation of high activity in subcutaneous adipose tissue demonstrated the advantage of using PET-CT apparatus. The high activity in liver tumors, TACE may be used for dose-reference marker of the proton beam irradiation.

In the result, it was suggested that the events of the activity detected by use of the BOLPs provided enough data for reconstruction of the PET image. The clinical use of this information about the positron-emitting nuclei generated will be important for promoting proton treatment with higher accuracy in the future. For that reason, it will be necessary to much-improve the accuracy of the measured and calculated activity for the innovative proton therapy in which the irradiation position is especially controlled within a few mm in the treatment site with high accuracy of the patient positioning such as head and neck.

Acknowledgments We greatly thank the staff members of the Proton Radiotherapy Department of the National Cancer Center, Kashiwa, for their assistance, and the members of SHI Accelerator Service Ltd. and Accelerator Engineering Inc. for operation of the proton apparatus. We are grateful to the reviewers and editors of this Journal for their comments and advices, and thank the other office staffs for their supports.

References

1. Chu WT, Ludewigt BA, Renner TR. Instrumentation for treatment of cancer using proton and light-ion beams. Rev Sci Instrum. 1993;64(8):2055–122.
2. Bennett GW, Goldberg A, Levine G, Guthy J, Balsamo J. Beam localization via 15O activation in proton radiation therapy. Nucl Instr Meth. 1975;125:333–8.
3. Bennett GW, Archambeau JO, Archambeau BE, Meltzer JI, Wingate CL. Visualization and transport of positron emission from proton activation in vivo. Science. 1978;200:1151–3.
4. Oelfke U, Lam G, Atkins M. Proton dose monitering with PET: quantiative studies in Lucite. Phys Med Biol. 1996;41:177–96.
5. Litzenberg DW, Roberts DA, Lee MY, Pham K, Vander Molen AM, Ronningen R, et al. On-line monitoring of radiotherapy beams: experimental results with proton beams. Med Phys. 1999;26(6):992–1006.
6. Parodi K, Enghardt W. Potential application of PET in quality assuarnce of proton therapy. Phys Med Biol. 2000;45:N151–6.
7. Nishio T, Ogino T, Shimbo M, Katsuta S, Kawasaki S, Murakami T, et al. Distributions of β^+ decayed nucleus produced from the target fragment reaction in (CH_2) n and patient liver targets by using a proton beam for therapy. Abstracts of the XXXIV PTCOG MEETING in Boston; 2001. pp. 15–6.
8. Parodi K, Enghardt W, Haberer T. In-beam PET measurements of β^+ radioactivity induced by proton beams. Phys Med Biol. 2002;47:21–36.
9. Hishikawa Y, Kagawa K, Murakami M, Sasaki H, Akagi T, Abe M. Usefulness of positron-emission tomographic images after proton therapy. Int J Rad Oncol Biol Phys. 2002;53:1388–91.
10. Enghardt W, Crespo P, Fiedler F, Hinz R, Parodi K, Pawelke J, et al. Dose quantification from in-beam positron emission tomography. Radiother Oncol. 2004;73(Suppl. 2):S96–8.
11. Nishio T, Sato T, Kitamura H, Murakami K, Ogino T. Distributions of β^+ decayed nuclei generated in the CH_2 and H_2O

targets by the target nuclear fragment reaction using therapeutic MONO and SOBP proton beam. Med Phys. 2005;32(4):1070–82.
12. Parodi K, Ponisch F, Enghardt W. Experimental study on the feasibility of in-beam PET for accurate monitoring of proton therapy. IEEE Trans Nucl Sci. 2005;52:778–86.
13. Nishio T, Ogino T, Nomura K, Uchida H. Dose-volume delivery guided proton therapy using beam ON-LINE PET system. Med Phys. 2006;33(11):4190–7.
14. Photon, Electron, Proton and Neutron Interaction Data for Body Tissues (ICRU Report 46). pp. 11–3.
15. Iljinov AS, Semenov VG, Semenova MP, Schopper H. Interactions of protons with nuclei (supplement to I/13a, b, c), (Landolt-Bornstein New Series. 1994).
16. Goldharber AS. Statistical models of fragmentation processes. Phys Lett. 1974;53B:306–8.
17. Winger A, Sherrill BM. Morrissey. INTENSITY: acomputer program for the estimation of secondary beam intensities from a projectile fragment separator. Nucl Instrum Methods. 1992;B70:380–92.
18. Nishio T. Proton therapy facility at National Cancer Center, Kashiwa, Japan. J At Energy Soc. 1999;41(11):1134–8.
19. Tachikawa T, Sato T, Ogino T, Nishio T. Proton treatment devices at National Cancer Center (Kashiwa). Radiat Indust. 1999;84:48–53.
20. Nishio T, Kataoka S, Tachibana M, Matsumura K, Uzawa N, Saito H, et al. Development of a simple control system for uniform proton dose distribution in a dual-ring double scattering system. Phys Med Biol. 2006;51:1249–60.
21. Nishio T, Ogino T, Sakudo M, Tanizaki N, Yamada M, Nishida G, et al. Present proton treatment planning system at National Cancer Center Hospital East. Jpn J Med Phys Proc. 2000;20(Suppl. 4):174–7.
22. Boellaard R, Lingen AV, Lammertsma AA. Experimental and clinical evaluation of iterative reconstruction (OSEM) in dynamic PET: quantitative characteristics and effects on kinetic modeling. J Nucl Med. 2001;42:808–17.
23. Tomitani T, Pawelke J, Kanazawa M, Yoshikawa K, Yoshida K, Sato M, et al. Washout studies of ^{11}C in rabbit thigh muscle implanted by secondary beams of HIMAC. Phys Med Biol. 2003;48:875–89.
24. Mizuno H, Tomitani T, Kanazawa M, Kitagawa A, Pawelke J, Iseki Y, et al. Washout measurement of radioisotope implanted by radioactive beams in the rabbit. Phys Med Biol. 2003;48:2269–81.

Radiotherapy and Oncology xxx (2009) xxx–xxx

Contents lists available at ScienceDirect

Radiotherapy and Oncology

journal homepage: www.thegreenjournal.com

Original article

Relation between elective nodal failure and irradiated volume in non-small-cell lung cancer (NSCLC) treated with radiotherapy using conventional fields and doses

Naoko Sanuki-Fujimoto [a,*], Minako Sumi [a], Yoshinori Ito [a], Atsushi Imai [a], Yoshikazu Kagami [a], Ikuo Sekine [b], Hideo Kunitoh [b], Yuichiro Ohe [b], Tomohide Tamura [b], Hiroshi Ikeda [a]

[a] Department of Radiation Oncology, National Cancer Center Hospital, Japan
[b] Department of Thoracic Oncology and Internal Medicine, National Cancer Center Hospital, Japan

ARTICLE INFO

Article history:
Received 3 October 2008
Received in revised form 29 December 2008
Accepted 30 December 2008
Available online xxxx

Keywords:
Chemoradiotherapy
Elective nodal failure
Elective nodal irradiation
Non-small-cell lung carcinoma
Radiotherapy

ABSTRACT

Introduction: The role of elective nodal irradiation of non-small-cell lung cancer (NSCLC) patients treated with radiotherapy remains unclear. We investigated the significance of treating clinically uninvolved lymph nodes by retrospectively analyzing the relationship between loco-regional failure and the irradiated volume.

Methods: Between 1998 and 2003, patients with IA–IIIB NSCLC were treated with radiotherapy. The eligibility criteria for this study were an irradiation dose of 60 Gy or more and a clinical response better than stable disease. Typical radiotherapy consisted of 40 Gy/20 fr to the tumor volumes (clinical target volume of the primary tumor [CTVp], of the metastatic lymph nodes [CTVn], and of the subclinical nodal region [CTVs]), followed by off-cord boost to CTVp+n to a total dose 60–68 Gy/30–34 fr. The relationship between the sites of recurrence and irradiated volumes was analyzed.

Results: A total of 127 patients fulfilled the eligibility criteria. Their median overall and progression-free survival times were 23.5 (range, 4.2–109.7) and 9.0 months (2.2–109.7), respectively. At a median follow-up time of 50.5 months (range, 14.2–83.0) for the surviving patients, the first treatment failure was observed in 95 patients (loco-regional; 41, distant; 42, both; 12). Among the patients with loco-regional failure, in-field recurrence occurred in 38 patients, and four CTVs recurrences associated with CTVp+n failure were observed. No isolated recurrence in CTVs was observed.

Conclusions: In-field loco-regional failure, as well as distant metastasis, was a major type of failure, and there was no isolated elective nodal failure. Radiation volume adequacy did not seem to affect elective nodal failure.

Radiation therapy is an integral component of the multi-modal treatment of non-small-cell lung cancer (NSCLC). Recent phase III studies have demonstrated that concomitant chemoradiotherapy improves survival, and this has resulted in the general acceptance of concurrent chemoradiotherapy as one of the standard treatments for locally advanced NSCLC [1]. Despite the improved survival, however, most patients die from their disease as a result of local or distant failure.

Local failure remains a major challenge when treating NSCLC with radiotherapy. A number of studies of dose escalation to the gross tumor volume (GTV) have been conducted as a means of improving local control [2–5]. The conventional radiation fields for NSCLC typically encompass the entire mediastinum and ipsilateral hilum (elective nodal region) to deliver a dose of 40 Gy, even without evidence of disease in these areas, followed by a 20 Gy boost to the GTV. However, the conventional treatment has added considerable morbidity and can limit the dose escalation. In phase I–II dose escalation studies, there is a trend toward omitting the practice of elective nodal irradiation (ENI) after their experiences with toxicity, which is not based on direct evidence [2–5]. According to those studies, omitting ENI has not sacrificed treatment outcomes so far. They also analyzed patterns of recurrence in relation to irradiated volume in a dose escalation setting [6].

By contrast, the current literature provides limited information regarding patterns of failure when conventional fields and doses are used [7,8]. Since it is important to know whether loco-regional failure is within or outside the irradiation field, we retrospectively analyzed patterns of failure after radiation therapy for NSCLC, especially in regard to the relationship between local failure and irradiated volume.

Methods and materials

Patients

Between January 1998 and March 2003, 263 patients with newly diagnosed NSCLC were treated with thoracic radiation therapy,

* Corresponding author. Address: Department of Radiation Oncology, National Cancer Center Hospital, 1-1, Tsukiji 5-chome, Chuo-ku, Tokyo 104-0045, Japan.
E-mail address: nao5-tky@umin.ac.jp (N. Sanuki-Fujimoto).

0167-8140/$ - see front matter © 2009 Elsevier Ireland Ltd. All rights reserved.
doi:10.1016/j.radonc.2008.12.013